

What controls the [O III] $\lambda 5007$ line strength in active galactic nuclei?

Alexei Baskin^{*} and Ari Laor^{*}

Physics Department, Technion, Haifa 32000, Israel

2 December 2024

ABSTRACT

Active galactic nuclei (AGN) display an extreme range in the narrow emission line equivalent widths. Specifically, in the PG quasar sample the equivalent width of the narrow [O III] $\lambda 5007$ line has a range of > 300 ($< 0.5\text{\AA}$ to 157\AA), while the broad H β line, for example, has a range of ten only (23\AA to 230\AA). The strength of [O III] $\lambda 5007$ is modulated by the covering factor (CF) of the narrow line region (NLR) gas, its density (n_e), and ionization parameter (U). To explore which of these factors produces the observed large range in [O III] $\lambda 5007$ strength, we measure the strength of the matching narrow H β and [O III] $\lambda 4363$ lines, detected in 40 out of the 87 $z < 0.5$ PG quasars in the Boroson & Green sample. The photoionization code CLOUDY is then used to infer CF, n_e , and U in each object, assuming a single uniform emitting zone. We find that the range of CF (~ 0.02 – 0.2) contributes about twice as much as the range in both n_e and U towards modulating the strength of the [O III] $\lambda 5007$ line. The CF is inversely correlated with luminosity, but it is not correlated with L/L_{Edd} as previously speculated. The single zone [O III] $\lambda 5007$ emitting region is rather compact, having $R_{\text{NLR}} = 40L_{44}^{0.45}$ pc. These emission lines can also be fit with an extreme two zone model, where [O III] $\lambda 4363$ is mostly emitted by a dense ($n_e = 10^7 \text{ cm}^{-3}$) inner zone at $R_{\text{NLR}}^{\text{in}} = L_{44}^{0.5}$ pc, and [O III] $\lambda 5007$ by a low density ($n_e = 10^3 \text{ cm}^{-3}$) extended outer zone at $R_{\text{NLR}}^{\text{out}} = 750L_{44}^{0.34}$ pc. Such an extended [O III] $\lambda 5007$ emission should be well resolved by Hubble Space Telescope imaging of luminous AGN. Further constraints on the radial gas distribution in the NLR can be obtained from the spectral shape of the IR continuum emitted by the associated dust.

Key words: galaxies: active – quasars: emission lines – quasars: general.

1 INTRODUCTION

Active galactic nuclei (AGN) can show both broad ($\text{FWHM} \gtrsim 1000 \text{ km s}^{-1}$) and narrow ($\text{FWHM} \lesssim 1000 \text{ km s}^{-1}$) emission lines. While both lines are excited by the central ionizing continuum source, the broad lines arise from the immediate vicinity of the central massive black hole ($R \lesssim 0.1$ pc), and the narrow lines arise further out, sampling the host galaxy dynamics, and possibly chemical composition and gas distribution as well. The strength and profiles of the narrow emission lines were studied extensively over the past 30 years, revealing radial gradients in the density and ionization state of the gas, and some characteristic trends in the line profiles (e.g. Heckman et al. 1981; Osterbrock 1989; Peterson 1997; Vanden Berk et al. 2001).

One remarkable property of the narrow emission lines,

which has not been explored yet in detail, is their extreme range of equivalent widths (EWs). Specifically, in the Boroson & Green (1992, hereafter BG92) sample of 87 $z < 0.5$ quasars from the bright quasar survey (Schmidt & Green 1983), the narrow [O III] $\lambda 5007$ line ranges in EW from 157\AA to undetectable ($< 0.5 \text{\AA}$), i.e. by a factor of > 300 , while in contrast the EW of the broad H β line in the same sample ranges only over a factor of 10 (23 – 230\AA). The narrow line EW is mainly set by two factors, the covering factor (CF) of the photoionized gas at the narrow line region (NLR), and the line emissivity (assuming no foreground absorption). The CF is set by the spatial distribution of the gas at the NLR, and by the angular distribution of the illuminating ionizing radiation. The latter may be set by the continuum emission mechanism, or through obscuration further out (e.g. by the ‘torus’). The line emissivity for collisionally excited lines, such as [O III] $\lambda 5007$, is set by the gas electron density n_e , the gas temperature, and by the gas ionization state. The last two properties are set by the ionizing photon flux, or equivalently the ionization parameter ($U \equiv n_{\gamma}/n_e$,

^{*} E-mail: alexei@physics.technion.ac.il (AB); laor@physics.technion.ac.il (AL)

where n_γ is the density of H ionizing photons). *Which of the above factors produces the large range in EWs of the narrow emission lines?*

The purpose of this paper is to answer this question for the [O III] $\lambda 5007$ line. We have chosen this line since it is generally the strongest and least blended narrow emission line in AGN. Our approach is to measure the strength of the narrow [O III] $\lambda 4363$ and H β lines in a large sample of AGN, where the [O III] $\lambda 5007$ line was already measured. The [O III] $\lambda 4363$ /[O III] $\lambda 5007$ line ratio is mainly a measure of n_e , while the H β line is dominated by recombination and thus mostly sensitive to the CF of the gas. The combination of the three lines allows us to determine the CF, n_e , and U of the [O III] $\lambda 5007$ emitting gas, and thus find which factor most strongly modulates the strength of the line. This derivation relies on the simplifying assumption that H β , [O III] $\lambda 5007$, and [O III] $\lambda 4363$ originate in a single zone with homogeneous gas properties. We relax this assumption by also making an extreme two zone approximation, where [O III] $\lambda 5007$ is mostly emitted by an outer low density NLR component, and [O III] $\lambda 4363$ by an inner high density component, and again explore whether the strength of the [O III] $\lambda 5007$ line is mostly modulated by the CF or by the gas emissivity.

The [O III] $\lambda 5007$ line is one of the main components contributing to the set of strongly correlated AGN emission properties, so called ‘eigenvector 1’ (hereafter EV1, BG92). We therefore also briefly explore whether the physical parameters controlling the strength of [O III] $\lambda 5007$ are linked to other EV1 emission properties. The determination of U and n_e allows us to calculate the distance of the NLR from the central ionizing continuum source, R_{NLR} , and we also look for relations between R_{NLR} and other AGN properties. The paper is organized as follows, in Section 2 we provide a brief theoretical justification for the set of lines used in this analysis, and explain how the NLR parameters are derived. In Section 3 we describe the sample used and the narrow line measurement procedure. The results are described and discussed in Section 4, and the main conclusions are provided in Section 5.

2 THEORETICAL APPROACH

The [O III] $\lambda 5007$ and [O III] $\lambda 4363$ lines are particularly useful for constraining T and n_e of the NLR gas which produces the [O III] line emission. Both lines arise from the same element, eliminating abundance effects. Furthermore, they both arise from the same ionization state, eliminating ionization level corrections. Both lines arise through collisional excitation, and although they correspond to similar transition energy, they differ in two respects. First, [O III] $\lambda 5007$ arises from excitation to the 1D_2 level, located 2.51 eV above the ground (3P_0) level, while [O III] $\lambda 4363$ arises from excitation to the 1S_0 level, 5.35 eV above the ground level. Thus, their ratio is a useful temperature diagnostic when $kT \lesssim 10$ eV. In addition, the two transitions have different radiative decay rates, leading to critical densities for collisional deexcitation of $7.0 \times 10^5 \text{ cm}^{-3}$ for [O III] $\lambda 5007$ and $3.3 \times 10^7 \text{ cm}^{-3}$ for [O III] $\lambda 4363$. Thus, the [O III] $\lambda 4363$ /[O III] $\lambda 5007$ line ratio is also a useful density diagnostic, when the density is not much above or below the two critical densities (e.g. Oster-

brock 1989). An additional advantage of the [O III] $\lambda 5007$ line is that it is typically the main coolant of the NLR (amounting to as much as ~ 50 per cent of the total cooling), and thus its absolute intensity is only a weak function of the O abundance (through the metalicity dependence of the gas temperature).

Figure 1 presents curves of constant $\log [\text{O III}] \lambda 4363/[\text{O III}] \lambda 5007$ photon flux ratio as a function of the electron density and temperature. The calculations are based on a 6-levels [O III] model (excitations to levels above the 6th level, 1S_0 , do not contribute significantly to the two [O III] lines at the relevant temperatures). The level energies were obtained from Moore (1993, p. 267), and radiative transition probabilities and mean collision strengths from Pradhan & Peng (1995, table 1 there, for $T = 10^4 \text{ K}$, relevant here)¹. The figure demonstrates the weaker dependence of the line ratio on n_e at the lowest n_e , and weaker dependence on T as the highest T .

In photoionized gas it is more natural to use U , which is often a free parameter in photoionization calculations, rather than T which is set by U and n_e through detailed photoionization calculations. Fig. 1 presents the dependence of T on n_e and U , as deduced from the photoionization code CLOUDY (Ferland et al. 1998). It demonstrates the weak dependence of T on n_e , at a given U , and the overall small range in T ($1.25 \times 10^4 \text{ K}$) when U varies from 10^{-4} to 10^{-1} . Assuming a uniform n_e gas, the measured value of [O III] $\lambda 4363/[\text{O III}] \lambda 5007$ (corresponding to a certain curve in Fig. 1) yields the allowed range of n_e as a function of the range in U . E.g., if the measured line ratio is 0.1, then the implied density is $n_e = 10^{5.75}$ to $10^{6.3} \text{ cm}^{-3}$, for $U = 10^{-1}$ to 10^{-4} . As can be seen in Fig. 1, the allowed range in n_e increases as the line ratio gets smaller.

Breaking the n_e , U , degeneracy requires an additional line. The optimal line for that purpose is H β . It is a nearly pure recombination line at the expected NLR conditions (where collisional and optical depth effects should be small), and thus its intensity provides an estimate of the fraction of ionizing radiation intercepted by the NLR, i.e. the NLR CF. The [O III] $\lambda 5007/\text{H}\beta$ ratio provides the additional constraint on n_e and U , required to break the degeneracy. The H β EW, together with the EW of [O III] $\lambda 5007$, and [O III] $\lambda 4363$, allow us to determine n_e , U , and the CF of the [O III] emitting gas in the NLR. From the observational aspect the H β line is also optimal, as it is located close to the two [O III] lines, allowing all three lines to be obtained in a single spectrum, minimizing systematic measurement errors. Also, the close wavelength proximity of the lines minimizes dust reddening effects on the measured line ratios.

As noted above, we use the photoionization code CLOUDY to calculate the strength of [O III] $\lambda 5007$, [O III] $\lambda 4363$, and H β , as a function of n_e (from 10^3 cm^{-3} to 10^8 cm^{-3}), U (from 10^{-4} to 10^{-1}), and the CF. The additional input model parameters for CLOUDY are a slab geometry with a total column of 10^{23} cm^{-2} , ISM abundances with grains, and a standard Mathews & Ferland (1987; hereafter MF) AGN continuum with a break at $1 \mu\text{m}$ (Ferland

¹ Two collision strengths, $\Omega(2p^3 \text{ } ^5S_2^0, 2p^2 \text{ } ^1S_0)$ and $\Omega(2p^3 \text{ } ^5S_2^0, 2p^2 \text{ } ^1D_2)$, were not available, and we therefore assume are equal to 1.

et al. 1998). The results are not sensitive to the assumed column since the dust opacity strongly suppresses line emission from columns beyond 10^{21} cm^{-2} (Laor & Draine 1993, hereafter LD). The effect of the ionizing continuum shape is explored by calculating the model results again with a different ionizing spectrum, as further described in Section 4.

Figure 2 presents the calculated line flux ratios and EW as a function of n_e for different values of U . The upper panel shows the $[O\text{ III}]\lambda 5007/\text{H}\beta$ flux ratio. This ratio decreases with increasing n_e due to collisional suppression of the $[O\text{ III}]\lambda 5007$ line at $n_e > 10^{5.85}$. The ratio increases with U at low U , as the fractional abundance of O III increases, and starts decreasing at $\log U > -1.5$, as O gets ionized beyond O III (the dust opacity suppresses emission from deeper layers where O is less ionized). The middle panel shows the $[O\text{ III}]\lambda 4363/[O\text{ III}]\lambda 5007$ flux ratio. This ratio is mostly set by n_e due to the different n_{crit} of the two lines, as discussed above. The weak dependence on U results from the weak dependence of T on U (Fig. 1). The lower panel shows the $\text{H}\beta$ EW for a CF = 1. At low U the $\text{H}\beta$ EW is independent of n_e and U , as expected for a pure recombination line. At $\log U > -2.5$ the $\text{H}\beta$ EW starts decreasing due to the increasing suppression of the line emission by absorption in dust within the ionized gas (Voit 1992; LD; Netzer & Laor 1993; Ferguson et al. 1997; Dopita et al. 2002).

Figure 3 presents theoretical curves of the $[O\text{ III}]\lambda 5007/\text{H}\beta$ flux ratio as a function of the $[O\text{ III}]\lambda 4363/[O\text{ III}]\lambda 5007$ flux ratio for different values of n_e and U . This plot allows one to transform the two measured line ratios in a given object to the corresponding values of n_e and U in that object. The third parameter, the CF, is then set by the EW of either one of the three lines. There is a one to one transformation from the $[O\text{ III}]\lambda 5007/\text{H}\beta$ versus $[O\text{ III}]\lambda 4363/[O\text{ III}]\lambda 5007$ coordinate to the n_e versus U coordinate, as long as $\log U \lesssim -2.2$. Above that value there are two sets of solutions, one having $\log U < -1.5$, and the other $\log U > -1.5$, for a given set of $[O\text{ III}]\lambda 5007/\text{H}\beta$ and $[O\text{ III}]\lambda 4363/[O\text{ III}]\lambda 5007$ values (see Fig. 3). The presence of two solutions results from the non-monotonic dependence of $[O\text{ III}]\lambda 5007/\text{H}\beta$ on U , mentioned above (Fig. 2, upper panel). The two solutions correspond to different CF values (the larger U requires a larger CF to produce the observed $\text{H}\beta$ EW, Fig. 2 lower panel). Obtaining a unique solution requires additional constraints on U or CF. As further described in Section 3, almost none of our objects happens to lie within the degenerate solution regime. However, note that photoionization models with $\log U > -1$, not explored here, produce lower $[O\text{ III}]\lambda 5007/\text{H}\beta$ ratios, which will be degenerate with some $\log U \lesssim -2.2$ solutions. Such high U models require a high CF, and they imply strong high ionization narrow lines, which we do not study here.

The above analysis is within the single zone approximation, i.e. all three lines are assumed to originate in gas with a given set of n_e , U and CF. In reality, there is likely to exist a distribution of values for these three parameters in the NLR, in which case the relative line strength will be a function of position in the NLR (e.g. Ferguson et al. 1997). The assumption of a single zone with uniform gas properties may not yield representative mean values in this case. To explore the effects of a non uniform cloud population, we repeated the analysis assuming two populations of clouds with very

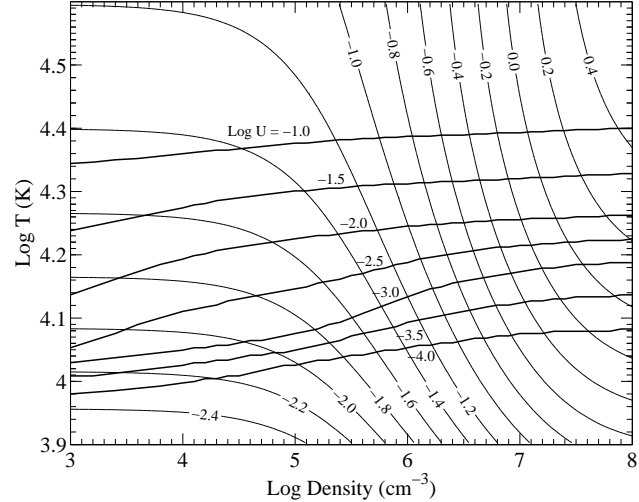


Figure 1. Curves of constant $\log [O\text{ III}]\lambda 4363/[O\text{ III}]\lambda 5007$ photons ratio as a function of $\log n_e$ and $\log T$ for a 6-levels collisionally excited O III. The thick lines represent $T(n_e)$ for different values of U , as calculated by the photoionization code CLOUDY. Note the weak dependence of T on n_e at a given U .

different $[O\text{ III}]\lambda 5007$ and $[O\text{ III}]\lambda 4363$ emissivities. The first population is assumed to have a density $n_e = 10^7\text{ cm}^{-3}$, and thus produces a high $[O\text{ III}]\lambda 4363/[O\text{ III}]\lambda 5007$ ratio, and the second population is assumed to have $n_e = 10^3\text{ cm}^{-3}$, and thus produces a ratio lower by a factor of ~ 100 (Fig. 3). Most of the $[O\text{ III}]\lambda 4363$ emission is expected to come from the first population of clouds, and most $[O\text{ III}]\lambda 5007$ from the second. Such a “two zone model” has six free parameters (n_e , U , and CF for each zone), and three need to be set since we only have three constraints (the EWs of $\text{H}\beta$, $[O\text{ III}]\lambda 5007$, and $[O\text{ III}]\lambda 4363$). The additional parameter we fix is $\log U = -1$ for the $n_e = 10^7\text{ cm}^{-3}$ zone, which implies this is an inner very compact zone. This rather high U is motivated by the mean spectral energy distribution (SED) of AGN, which indicates a significant covering factor of very hot dusty gas with a high ionization parameter. The dust temperature indicates it is located outside the BLR, but on scales smaller than the “typical” NLR. The lack of strong line emission from the associated gas implies $U \gg 10^{-2}$, to allow significant suppression of the line emission by the dust (Section 2). The remaining free parameters of the two zone model are the ionization parameter of the outer zone, U_{out} , and the covering factors of the inner and outer zones, CF_{in} , CF_{out} , these are set as described below in Section 3.4.

3 DATA ANALYSIS

3.1 The data set

For the analysis we use the BG92 sample mentioned above (Section 1). This sample extends in luminosity from Seyfert galaxies with $\nu L_\nu = 3.3 \times 10^{43}\text{ erg s}^{-1}$ (calculated at rest frame 3000 Å using the continuum fluxes in Neugebauer et al. 1987, assuming $H_0 = 80\text{ km s}^{-1}\text{ Mpc}^{-1}$, $\Omega_0 = 1.0$), to luminous quasars at $\nu L_\nu = 1.4 \times 10^{46}\text{ erg s}^{-1}$. This is a complete and well defined sample, selected based on (blue) color and (point like) morphology, independently of the emission

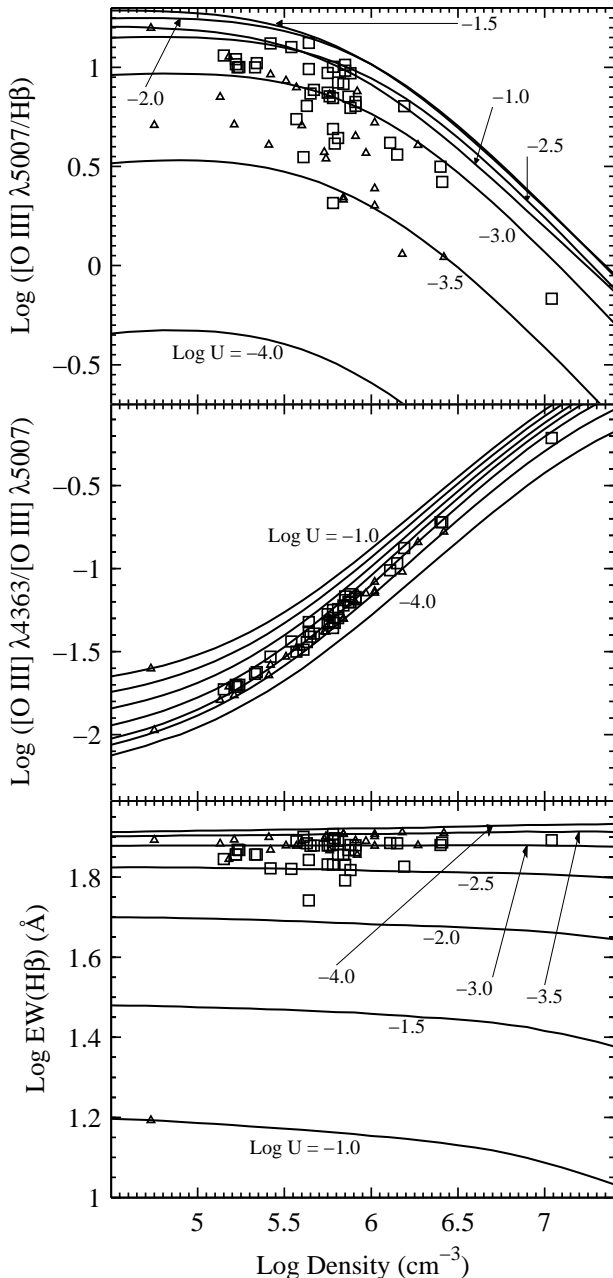


Figure 2. The solid lines present the dependence of $[\text{O III}] \lambda 5007/\text{H}\beta$ (upper panel), $[\text{O III}] \lambda 4363/[\text{O III}] \lambda 5007$ (middle panel), and $\text{H}\beta$ EW (lower panel) on n_e , at given values of U , as calculated by CLOUDY. The square boxes represent objects with detections, and the triangles objects with an upper limit on the $[\text{O III}] \lambda 4363$ EW, i.e. an upper limit on n_e . In the lower panel the calculated $\text{H}\beta$ EW is for $\text{CF} = 1$, and for each object we therefore plotted the observed $\text{H}\beta$ EW divided by the inferred CF .

line strengths and profiles (subject to the condition that broad emission lines are present).

Optical observations of the $\text{H}\beta$ region of the 87 objects are described in BG92, and were kindly provided by T. Boroson (private communication). These spectra do not extend down to $[\text{O III}] \lambda 4363$ in all objects, and we therefore supplemented the BG spectra by optical spectra from Shang

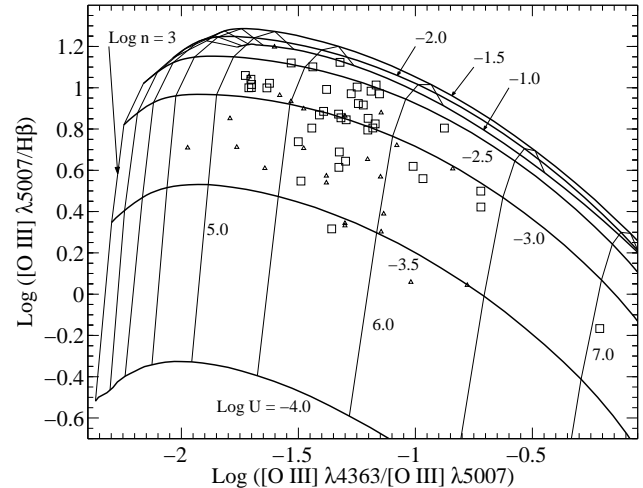


Figure 3. The theoretical and measured relation between $[\text{O III}] \lambda 5007/\text{H}\beta$ and $[\text{O III}] \lambda 4363/[\text{O III}] \lambda 5007$. The solid lines represent curves of constant n_e and constant U , as calculated by CLOUDY. The object symbols are as in Fig. 2.

et al. (2003), kindly provided by Z. Shang (private communication) which also provide a higher S/N in some cases². The final sample contains 78 objects with spectra which contain the $[\text{O III}] \lambda 4363$ region. The spectra were corrected for reddening, redshift, and possible slit losses, as described in Baskin & Laor (2004, hereafter BL04, Section 2.2 there).

3.2 The Fe II subtraction

The $[\text{O III}] \lambda 4363$ line is generally very weak, and its measurement requires a careful subtraction of the Fe II emission multiplets. We used the I Zw 1 Fe II template, kindly provided by T. Boroson, to subtract the Fe II lines from the spectra (see Section 2.2 in BL04 for further details concerning the subtraction procedure).

The Fe II template was constructed by subtracting all the none Fe II emission from the observed spectrum of I Zw 1. However, this also requires estimates of the relative contributions of Fe II and $[\text{O III}] \lambda 4363$ near 4363Å, which may not be accurate, and could lead to biased estimates of the $[\text{O III}] \lambda 4363$ strength in the Fe II subtracted spectra. To check the accuracy of the Fe II subtraction, we also used the more theoretically motivated Fe II template of I Zw 1, independently constructed by Véron-Cetty, Joly & Véron (2004), kindly provided by M. Véron-Cetty. The BG92 template is rather smooth and featureless around 4363Å, and the Véron-Cetty et al. template has a sharp feature redward of 4363Å, but much weaker emission at 4363Å, compared to BG92. The Véron-Cetty et al. compilation of expected allowed and forbidden Fe II emission lines indicates no significant feature near 4363Å. There was almost no effect on the $[\text{O III}] \lambda 4363$ profile in I Zw 1 when using either the Véron-Cetty et al. template or the BG92 template to subtract the Fe II emission. We therefore conclude that improper

² The spectra obtained from Shang et al. (2003) are of PG 0953+414, PG 1216+069, PG 1322+659, PG 1427+480, PG 1512+370 and PG 1543+489.

Fe II subtraction is unlikely to significantly bias our measurements of the $[O\text{ III}]\lambda 4363$ line. In our analysis we used the empirically derived BG92 Fe II template.

3.3 The measurement procedure

As noted above, there is likely to exist a distribution of n_e , U , and CF values for the $[O\text{ III}]$ emitting gas in the NLR. To ensure as much as possible that the measured $H\beta$ and $[O\text{ III}]\lambda 4363$ emission originates in the same gas which produces the $[O\text{ III}]\lambda 5007$ emission, we use the $[O\text{ III}]\lambda 5007$ profile as a template for measuring the $H\beta$ and $[O\text{ III}]\lambda 4363$ lines. This ensures that all three lines originate in gas with the same line of sight velocity distribution, although it does not necessarily guarantee they all originate in NLR gas clouds with the same distribution of emission properties.

In each object we subtracted the maximum allowed scaled $[O\text{ III}]\lambda 5007$ profile which does not produce a dip in the broad $H\beta$ line and in the $H\gamma+ [O\text{ III}]\lambda 4363$ blend, as determined by eye inspection. The subtraction was performed as follows. Both the $[O\text{ III}]\lambda 5007$ line and either $[O\text{ III}]\lambda 4363$ or $H\beta$ were transformed from wavelength scale to velocity scale, using z measured from the $[O\text{ III}]\lambda 5007$ peak (T. Boroson, private communication, listed in BL04). Then, the maximal c in the term $f_{\text{line}}(v) - c \times f_{5007}(v)$ was searched, where ‘line’ is either $H\beta$ or $[O\text{ III}]\lambda 4363$, such that the subtraction of the scaled $[O\text{ III}]\lambda 5007$ profile will not produce a dip in the measured line. The measured narrow line component equals the scaled $[O\text{ III}]\lambda 5007$ line, $f_{\text{line}}(v) = c \times f_{5007}(v)$. To calculate the line EW the line profile $f_{\text{line}}(v)$ was transformed back to wavelength dependence $f_{\text{line}}(\lambda)$, integrated over λ , and divided by the continuum flux density at 4861 Å (the same wavelength used by BG92). The flux density at 4861 Å was measured by fitting a local power-law continuum to each spectrum between ~ 4600 Å and ~ 5100 Å. We measured the line EW directly, rather than infer it from the $[O\text{ III}]\lambda 5007$ EW measured by BG92 and the value of c , since the $[O\text{ III}]\lambda 5007$ profile deduced here may not be identical to the one assumed by BG92 due to possibly different definitions of the continuum underlying $[O\text{ III}]\lambda 5007$.

To determine whether the measured line flux is significant or not, we need to evaluate the standard deviation, σ , of the flux measurement. We first measured the RMS of the flux density between 4500\AA and 4600\AA ³, multiplied the RMS by the wavelength width of a pixel (to convert flux density to flux), and then multiplied it by the square-root of the number of pixels in the full width at zero intensity of the $[O\text{ III}]\lambda 5007$ profile, to get σ . A measured line flux was accepted as significant if it is $> 3\sigma$. Following BG92, we also adopted an EW of 0.5 Å as the lower detection limit (accounting for the minimum likely level of systematic errors). After exclusion of objects with an unmeasurable $H\beta$ narrow component, and an unmeasurable $[O\text{ III}]\lambda 4363$, the remaining sample contained 40 objects where all three lines are detected.

Figure 4 shows four representative cases of the $[O\text{ III}]\lambda 5007$ profile subtraction from the $H\gamma+ [O\text{ III}]\lambda 4363$ blend. The two left panels present objects where the

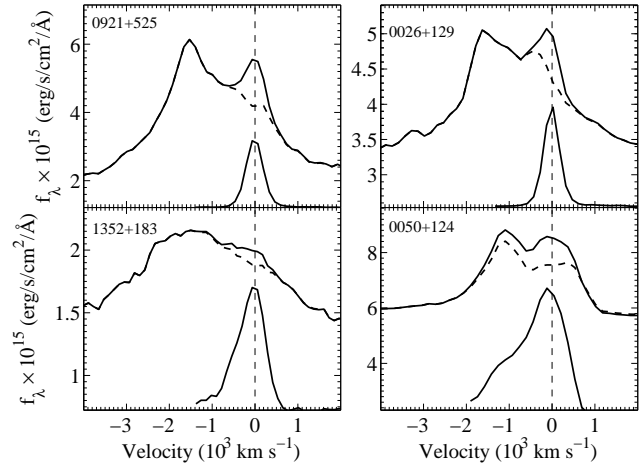


Figure 4. The $H\gamma$ and $[O\text{ III}]\lambda 4363$ blend before (top continuous line) and after (dashed line) subtraction of the scaled $[O\text{ III}]\lambda 5007$ profile, and the $[O\text{ III}]\lambda 5007$ profile (scaled by an arbitrary factor for presentation; bottom continuous line). The name of the object is indicated in each panel. Upper-left, the significance of the measurement is 18.6σ . Lower-left, the significance is 3.6σ . The two right panels demonstrate a broad residual $[O\text{ III}]\lambda 4363$ component that often remains (see text).

$[O\text{ III}]\lambda 4363$ emission is rather well fit using the $[O\text{ III}]\lambda 5007$ profile. The upper left panel is a clear 18.6σ detection, and the lower left one a marginally acceptable detection at 3.6σ . The two right panels in Fig. 2 demonstrate cases where a broad residual $[O\text{ III}]\lambda 4363$ component remains after subtraction of the scaled $[O\text{ III}]\lambda 5007$ profile. Such a broad residual component often remains, and it most likely indicates an inner higher density extension of the NLR, where the density is higher than the $[O\text{ III}]\lambda 5007$ critical density but it is lower than the critical density of $[O\text{ III}]\lambda 4363$. Such an inner, higher velocity, extension of the NLR would contribute to the $[O\text{ III}]\lambda 4363$ line and not to the $[O\text{ III}]\lambda 5007$ line (Nagao et al. 2001). This demonstrates that making inferences based on the total $[O\text{ III}]\lambda 5007$ and $[O\text{ III}]\lambda 4363$ line fluxes, rather than matched profile fluxes, could lead to inaccurate results.

3.4 The inferred NLR parameters

Table 1 presents the narrow “ $[O\text{ III}]\lambda 5007$ -like” $H\beta$ and $[O\text{ III}]\lambda 4363$ EW, measured as described above. We also list in Table 1 the $[O\text{ III}]\lambda 5007$ EW from BG92 (the Shang et al. spectra yielded consistent values). Column 1 lists the name of the object, columns 2 and 3 list the measured $H\beta$ EW in units of Å and its significance in units of σ . Column 4 lists the $[O\text{ III}]\lambda 5007$ EW in units of Å, as reported by BG92. Columns 5 and 6 list the measured $[O\text{ III}]\lambda 4363$ EW and its significance. Column 7 lists $\log \nu L_\nu$ at 4861 Å in units of 10^{44} erg s^{-1} , which allows a quick conversion of line EW to line luminosities. Columns 8, 9 and 10 list the inferred NLR parameters, $\log U$, $\log n_e$ (in units of cm^{-3}), and CF (in per cent) for the single-zone model. Finally, columns 11, 12 and 13 list the CF_{in} (in per cent), $\log U_{\text{out}}$ and CF_{out} (in per cent) for the two-zones model.

To infer U , n_e and CF we calculated theoretical values of the $H\beta$ flux, and $[O\text{ III}]\lambda 5007/H\beta$ and

³ Seven spectra have a feature in this range, and thus a slightly different range was chosen for them.

Table 1. The measured emission line parameters and the inferred NLR parameters.

Object (1)	H β		[O III] λ5007		[O III] λ4363		νL_ν (7)	Single zone			Two zones		
	EW (2)	S/N (3)	EW (4)	S/N (5)	EW (6)	S/N (8)		U (8)	n (9)	CF (10)	CF _{in} (11)	U_{out} (12)	CF _{out} (13)
0003+158	1.96	20.9	26	1.24	16.5	1.579	-2.2	5.64	3.6	4.8	-1.50	4.7	
0003+199	5.34	22.9	22	1.04	6.8	-0.267	-3.3	5.79	6.8	4.8	-3.18	6.1	
0007+106	4.19	16	42	0.84	4.4	0.407	-2.9	5.24	5.7	2.8	-2.45	5.8	
0026+129	3.10	34.9	29	1.54	21.2	0.804	-2.6	5.75	4.6	6.9	-2.23	3.9	
0049+171	15.55	18.8	97	6.07	10.9	-0.509	-3.0	5.88	20.5	28.9	-2.85	16.4	
0050+124	6.97	41.4	22	4.19	27.5	0.312	-3.0	6.40	9.2	21.4	-3.22	5.6	
0052+251	3.90	29.9	30	1.22	10.3	0.808	-3.0	5.67	5.2	5.4	-2.68	4.6	
0838+770	3.58	8.8	13	1.40	4.4	0.356	-3.1	6.15	4.7	7.0	-3.20	3.5	
0921+525	13.00	33.3	83	5.46	18.6	-0.659	-3.0	5.91	17.2	26.0	-2.80	13.5	
0923+129	7.04	24.7	31	1.56	8.2	-0.579	-3.2	5.81	9.1	7.3	-3.15	8.1	
0934+013	7.29	22.6	51	2.58	11.7	-0.603	-3.0	5.78	9.6	11.9	-2.75	8.2	
0953+414	1.87	10.0	18	1.16	7.2	1.033	-2.6	5.85	2.8	5.3	-2.01	2.3	
1001+054	2.65	5.4	7	1.33	3.2	0.480	-3.1	6.41	3.4	6.8	-3.34	2.3	
1048+342	2.72	5.9	28	1.90	5.5	1.235	-2.4	5.85	4.4	8.4	-1.71	4.4	
1100+772	3.90	15.8	41	0.98	4.4	1.276	-2.8	5.34	5.4	3.5	-2.32	5.6	
1119+120	2.66	23.0	19	0.91	9.7	-0.140	-3.0	5.76	3.5	4.2	-2.73	3.0	
1126-041	3.47	12.4	19	0.60	3.2	0.021	-3.2	5.57	4.5	2.6	-3.05	4.1	
1149-110	4.64	16.7	33	2.07	9.5	-0.392	-2.9	5.87	6.3	9.8	-2.66	4.9	
1151+117	1.33	17.1	11	0.66	10.6	0.456	-2.8	5.84	1.9	3.1	-2.44	1.5	
1202+281	5.64	37.3	36	1.30	9.8	0.386	-3.1	5.63	7.4	5.7	-2.93	6.6	
1229+204	1.94	10.9	19	0.79	6.5	0.067	-2.7	5.64	2.8	3.4	-2.26	2.6	
1244+026	8.21	28.1	17	0.75	3.5	-0.454	-3.5	5.78	10.2	3.5	-3.51	9.6	
1302-102	2.16	12.8	9	0.88	5.5	1.510	-3.1	6.11	2.8	4.4	-3.13	2.1	
1307+085	3.18	14.7	32	1.80	11.8	0.716	-2.6	5.78	4.7	8.0	-2.01	4.2	
1309+355	2.55	18.0	19	0.89	7.1	0.756	-3.0	5.75	3.4	4.1	-2.68	2.9	
1310-108	8.24	39.2	77	5.41	30.6	-0.637	-2.5	5.88	12.5	24.8	-2.01	10.0	
1341+258	1.90	9.8	14	0.54	4.1	-0.053	-3.0	5.65	2.5	2.4	-2.73	2.2	
1351+236	2.46	11.2	12	0.57	3.0	-0.204	-3.2	5.78	3.2	2.6	-3.09	2.8	
1351+640	3.70	20.6	31	1.77	11.3	0.515	-2.8	5.81	5.2	8.2	-2.44	4.1	
1352+183	1.57	4.8	10	1.33	3.6	0.432	-2.6	6.19	2.3	6.6	-2.34	1.2	
1411+442	2.25	9.9	15	1.01	6.5	0.279	-2.9	5.91	3.1	4.8	-2.73	2.3	
1425+267	3.61	20.0	36	0.84	4.9	1.301	-2.8	5.33	5.0	3.0	-2.42	5.0	
1501+106	5.58	35.6	64	1.20	10.9	0.016	-2.7	5.15	8.0	3.6	-2.22	8.8	
1512+370	5.50	20.9	57	1.14	5.2	0.958	-2.8	5.22	7.7	3.8	-2.39	7.9	
1519+226	5.87	8.6	4	2.45	4.8	0.265	-3.2	7.04	7.5	12.8	-3.96	5.4	
1534+580	5.99	48.3	79	2.33	25.3	-0.542	-2.5	5.42	9.0	7.8	-1.75	12.5	
1535+547	4.53	22.0	16	0.52	4.3	-0.286	-3.4	5.61	5.7	2.3	-3.27	5.4	
1545+210	2.61	11.2	33	1.20	6.5	1.093	-2.5	5.54	4.0	4.4	-1.72	5.3	
1612+261	14.28	74.3	157	3.11	23.1	0.332	-2.8	5.22	19.9	9.9	-2.28	21.6	
1704+608	2.70	15.2	27	0.52	3.4	1.410	-2.9	5.23	3.7	1.8	-2.46	3.7	

[O III] λ4363/[O III] λ5007 ratios using the photoionization code CLOUDY (v. 94.00). The calculations were made for a grid of models with $-4 \leq \log U \leq -1$ (in steps of 0.5), and $3 \leq \log n_e \leq 8$ (in steps of 0.1). The H β flux was converted to EW as follows. The choice of U and n_e corresponds to a given ionizing flux at the face of the photoionized slab, which is specified by the output of CLOUDY. We multiplied the H ionizing flux by 0.4 to get an approximate value for νf_ν at 4861 (deduced from the spectral shape in fig. 7 of LD), and divided it by 4861 to get the continuum f_λ at 4861 Å. The H β line flux from CLOUDY was then divided by this f_λ to get the predicted line EW for CF = 1. This procedure assumes a uniform spectral energy distribution (SED) in all objects, which may not correspond well with the range of observed SEDs in the PG sample quasars. However, as shown in Section 4.1.3, the likely range of SED shapes has only a minor effect on the deduced parameters.

For the single zone model we use the following algorithm

to infer U , n_e and CF from the H β EW, [O III] λ5007/H β and [O III] λ4363/[O III] λ5007 ratios.

- (i) Assume U , starting at $\log U = -4$.
- (ii) Calculate n_e from the observed [O III] λ4363/[O III] λ5007 ratio for the assumed U (Fig. 2, middle panel). The calculation is made using a linear interpolation scheme for \log [O III] λ4363/[O III] λ5007 versus $\log n_e$, when the observed [O III] λ4363/[O III] λ5007 value is between grid points.
- (iii) Calculate the theoretical [O III] λ5007/H β ratio for the assumed U , and the n_e calculated above (using a linear interpolation scheme as above).
- (iv) Calculate the theoretical [O III] λ5007 EW from the theoretical [O III] λ5007/H β ratio found above, and the observed H β EW.
- (v) Repeat steps (i)-(iv) changing $\log U$ from -4 to -1

in steps of 0.1 (using linear interpolations between U grid points).

(vi) Adopt as the solution the values of U and n_e which yield the smallest difference between the observed and theoretical [O III] $\lambda 5007$ EW, as calculated in step (iv).

(vii) Calculate the theoretical $H\beta$ EW for the U and n_e of the solution (Fig. 2, lower panel). Obtain CF by dividing the observed $H\beta$ EW by the theoretical one.

This procedure is effectively identical to the one described in Section 2. The differences between the observed and calculated [O III] $\lambda 5007$ EW are typically well below 10 per cent, which is generally within the [O III] $\lambda 5007$ EW measurement errors. The resulting best fit U, n_e and CF for each object are listed in Table 1.

As discussed in Section 2, in the two zone model we assume $n_e = 10^3 \text{ cm}^{-3}$ for the outer zone, and $n_e = 10^7 \text{ cm}^{-3}$ and $U = 0.1$ for the inner zone, leaving CF_{in} , CF_{out} and $\log U_{out}$ as the remaining three parameters to be set by the observations. The assumed n_e and U for the inner zone imply $\log [O III] \lambda 5007/H\beta = 0.2$, $\log [O III] \lambda 4363/[O III] \lambda 5007 = -0.04$ (see Fig. 3) and a calculated $H\beta$ EW of 12.21 Å for $CF_{in}=1$. We now iterate over the possible range of $\log U$ values for the outer zone. For each U value for the outer zone we calculate $[O III] \lambda 5007/H\beta$, $[O III] \lambda 4363/[O III] \lambda 5007$, and the $H\beta$ EW for $CF_{out}=1$. We now write two linear equations for the observed [O III] $\lambda 5007$ and [O III] $\lambda 4363$ EWs in a given object, as a function of the above line ratios, the calculated $H\beta$ EWs, and the two unknowns, CF_{in} and CF_{out} , which we solve for. The solution produces the correct observed $[O III] \lambda 5007/H\beta$, $[O III] \lambda 4363/[O III] \lambda 5007$ ratios by construction, and it also allows us to calculate the total expected $H\beta$ EW. The accuracy of the solution is measured by the difference between the observed and calculated total $H\beta$ EW. The U value which minimizes this difference (typically less than 10 per cent) is taken as the best fit solution for the given object.

4 RESULTS & DISCUSSION

4.1 The distribution of n_e and U values

4.1.1 The Single Zone Approximation

As shown in Table 1 and Fig. 2, the values of n_e of all 40 objects with detections (excluding one outlier, PG 1519+226) lie within a relatively small range (factor of ~ 5) around the critical density of [O III] $\lambda 5007$ (i.e. within $\log n_e = 5.85 \pm 0.7$). This is expected if there is a range of densities in the NLR, since the line emissivity per unit mass peaks close to the critical density, and thus the [O III] $\lambda 5007$ emissivity weighted mean density is expected to be at $n_e \sim n_{crit}$, unless the distribution of CF with density is heavily weighted towards very high or very low densities.

We also find that all objects (except one) lie at $\log U \leq -2.2$. A similar selection effect may be present here as well. As Fig. 2 (lower panel) shows, the $H\beta$ line emissivity per unit solid angle ($= EW/CF$) drops at $\log U > -2.5$ (due to dust suppression), and thus if there is a distribution of U values in the NLR with comparable values of CF, most of the $H\beta$ emission would originate in gas with $\log U < -2$. However,

at $\log U < -3.5$ the O III emission is suppressed because Oxygen becomes less ionized than O III. Thus, the combined effects of dust suppression and ion abundance leads to a relatively small range of U ($\log U = -3 \pm 0.5$) where both the [O III] lines and $H\beta$ are emitted efficiently.

In the above analysis we considered only objects where all the three narrow lines are detected. Ignoring upper limits may result in spurious trends or correlations. To explore that, we repeated the analysis described in Section 3 for all the objects where [O III] $\lambda 4363$ was not detected, assuming the line EW equals the upper limit value (the larger of the 3σ detection limit and 0.5 Å). These objects are also plotted in Figs. 2 and 3, and their distribution nearly overlaps the distributions of the detected objects. We also repeated the analysis arbitrarily assuming the [O III] $\lambda 4363$ EW is a factor of 10 lower than the upper limit. This leads to a tail of objects extending to $\log n_e = 3$, but the distribution of U values is not much affected. The extension to low n_e occurs because n_e is largely set by [O III] $\lambda 4363$ /[O III] $\lambda 5007$, while U is unchanged because it is largely set by [O III] $\lambda 5007/H\beta$, and it is nearly independent of the [O III] $\lambda 4363$ EW when [O III] $\lambda 4363/H\beta$ is low (Fig. 3).

4.1.2 The Two Zone Approximation

As described above, the two zone approximation we use assumes fixed values for n_e in the two zones, and a fixed U for the inner zone. For U_{out} we find $-4 \leq \log U_{out} \leq -1.5$, with most objects in the range of -3.5 to -2 . This distribution is offset to somewhat higher U values (by ~ 0.2) compared to the single zone approximation (Fig. 5).

4.1.3 Modified SED

Far UV observations of high z quasars (Zheng et al. 1997), together with soft X-ray observations of low z quasars (Laor et al. 1997), suggest a significantly softer ionizing SED than the one suggested by MF, which we used in the above analysis (but see Scott et al. 2004). To explore the possible role of the SED on the deduced NLR parameters we repeated the analysis in Section 3 with a modified softer SED, where we added a break at 1 Rydberg to a power-law slope of -1.5 extending to 70 Rydberg (~ 1 keV), as suggested by the far UV to soft X-ray composite of Laor et al. (1997). The rest of the SED remains unchanged.

The resulting softer SED values, n_e^s , and U^s , are very similar to those obtained with the harder MF SED. Apart from two outliers, where $\log U$ changed from ~ -2.3 to ~ -1 , due to the degeneracy of the U solution at high U (Fig. 3), for the other objects we find a very tight relation between U and U^s . Specifically, we find a best fit relation $\log U^s = 0.9 \log U - 0.24$, with an RMS scatter of 0.05, and a Spearman rank order correlation coefficient $r_s = 0.989$. This relation implies an average systematic offset of $\log U^s - \log U = -0.04$ to 0.11 , for $\log U = -2$ to -3.5 , which is well within the likely systematic and statistical errors in our solution for U . Similarly, for n_e^s we find $\log n_e^s = 1.02 \log n_e - 0.17$, an RMS scatter of 0.02, $r_s = 0.996$ (excluding the two outliers), and again a negligibly small offset of 0.07 to 0.03 for $\log n_e = 5$ to 7 . For the soft SED covering factor CF^s we get $CF^s = 1.00CF + 0.24$, with an RMS scatter of

only 0.01 and $r_s = 0.999$. Thus, CF^s is essentially perfectly correlated with CF, but it is offset to higher values by a factor of 1.74($=10^{0.24}$), as expected since the softer SED requires a larger CF to produce a given H β EW. Note that the exact absolute value of the best fit parameters, n_e , U , and CF, for each object are not crucial for our study of the modulation of the [O III] $\lambda 5007$ strength, and what mostly matters is the range of values for these parameters.

4.1.4 Comparison with Earlier Studies

Binette et al. (1996, and references therein) discuss evidence for the presence of significant contribution to the NLR emission from matter bounded gas. This component produces mostly high ionization lines, and it is invoked to explain the large relative strengths of the He II $\lambda 4686$ and C IV $\lambda 1549$ lines, seen in the NLR emission of Seyfert 2 galaxies (e.g. Ferland & Osterbrock 1986), as well as the strength of other lines not measured in our sample. The single and two zone models we use do not include such a matter bounded gas component. However, we suspect that such a component may not be required by our data, and the anomalous strength of He II $\lambda 4686$ may be interpreted differently, as further discussed below.

Binette et al. (1996) used a mean C IV $\lambda 1549$ /H β flux ratio of 12 ± 8 from Ferland & Osterbrock (1986). However, using the narrow C IV $\lambda 1549$ EW measurements available for our sample (BL04), we deduce a significantly lower mean value of 4.7 ± 6 , which is likely biased to large values as it does not exclude low significance level narrow C IV $\lambda 1549$ measurements. The weakness of the NLR C IV $\lambda 1549$ component in broad line AGN was already noted by Wills et al. (1993) in Hubble Space Telescope (*HST*) spectra of seven radio loud AGN⁴. The lower mean C IV $\lambda 1549$ /H β value is consistent with standard photoionization model predictions (e.g. Wills et al. 1993; Groves et al. 2004a), and thus there is no evidence from C IV $\lambda 1549$ for a matter bounded NLR component in our objects.

The mean He II $\lambda 4686$ /H β flux ratio in Seyfert 2 galaxies is 0.29 ± 0.1 (Ferland & Osterbrock, 1986). We measure a similar mean value of 0.30 ± 0.12 in 43 of our objects where a narrow “[O III] $\lambda 5007$ -like” He II $\lambda 4686$ is detectable. As shown in the extensive set of calculations by Groves et al. (2004a; 2004b), dusty photoionized gas models with $\log U \sim -2$ can produce He II $\lambda 4686$ /H $\beta \sim 0.3$ in ionization bounded gas. The models of Binette et al. (1996) do not include dust, and these produce lower He II $\lambda 4686$ /H β ratios, which lead Binette et al. to conclude that an additional population of matter bounded gas clouds must be present at the NLR. Dusty photoionized gas with $\log U \sim -2$ produces a higher He II $\lambda 4686$ /H β ratio since the H β line originates from deeper layers compared to He II $\lambda 4686$, and is thus more strongly suppressed by dust absorption. Most of the line emission in dusty photoionized gas originates within a surface layer with a column of $\leq 10^{21} \text{ cm}^{-2}$, where the dust opacity is ≤ 1 . The line emission from this surface layer mimics to

some extent the line emission from matter bounded, dust free photoionized gas, as invoked by Binette et al. (1996).

Dopita et al. (2002) calculated photoionization models for isobaric dusty gas, and proposed that the ionization parameter in such gas tends to a constant value, independent of the surface gas density, once radiation pressure dominates gas pressure. Dopita et al. further suggested this effect explains the small dispersion in the NLR line ratios ($\log [\text{O III}] \lambda 5007/\text{H}\beta \sim 0.9-1.2$ in their sample), and the implied nearly constant $\log U \sim -2$ in the NLR. However, here we find a much larger range ($\log [\text{O III}] \lambda 5007/\text{H}\beta \sim 0-1.1$, Fig. 3), which implies a correspondingly larger range in U . This argues against the effectiveness of the mechanism proposed by Dopita et al. to produce a fine tuned U in the NLR. We note in passing that the dusty isochoric CLOUDY model used here produces nearly identical line ratios to those reported by Groves et al. (2004a; 2004b) for isobaric dusty gas with significant radiation pressure. For example, Groves et al. find $\log [\text{O III}] \lambda 4363/[\text{O III}] \lambda 5007 = -1.65$ for $n_e = 10^3 \text{ cm}^{-3}$, $U = 0.1$, and solar abundance (Fig. 13 in Groves et al. 2004b), while we find -1.75 for the same parameters (Fig. 3). At $U = 10^{-4}$, where radiation pressure effects on dust are negligible, their model gives a ratio of -2.3 , and CLOUDY gives an essentially identical value of -2.36 .

4.2 Which parameter modulates most strongly the [O III] $\lambda 5007$ EW?

Figure 5 (upper panels) presents the dependence of the [O III] $\lambda 5007$ EW on U , n_e , and CF, for the single zone model. The [O III] $\lambda 5007$ EW ranges over a factor of 40 (4Å to 157Å) in our sample of 40 AGN with complete detections (compared with a range of > 300 in the complete sample of 87 objects). The [O III] $\lambda 5007$ EW is most strongly correlated with the CF. The Spearman rank order correlation coefficient, r_s , for the 40 detected objects is 0.699, which has a null probability of $\text{Pr} = 5.2 \times 10^{-7}$ (note that the distribution of the [O III] $\lambda 4363$ non detections is consistent with the distribution of the detections). The CF covers a range of about 10 (1.9 to 20.5 per cent, Table 1), and since the EW of all lines is linear with CF, the CF modulates the EW by a factor of 10, making it the dominant factor in modulating the [O III] $\lambda 5007$ EW.

The [O III] $\lambda 5007$ EW is also significantly correlated with n_e ($r_s = -0.473$, $\text{Pr} = 2 \times 10^{-3}$), though the [O III] $\lambda 4363$ non detections may affect the strength of this correlation if the true [O III] $\lambda 4363$ EW are well below the upper limits. The range of $n_e \sim 10^5 - 10^{6.5} \text{ cm}^{-3}$ amounts to a modulation of the [O III] $\lambda 5007$ EW by an additional factor of 3 (e.g. the $\log U = -2.5$ curve in Fig. 2, upper panel). Finally, the [O III] $\lambda 5007$ EW shows only a marginal correlation with U ($r_s = -0.384$, $\text{Pr} = 1.5 \times 10^{-2}$, not affected by upper limits). Although the range of $U \sim 10^{-3.5} - 10^{-2.2}$ modulates the [O III] $\lambda 5007$ EW by a factor of ~ 4 , its weak correlation with [O III] $\lambda 5007$ EW indicates it mostly contributes to the scatter in the previous two relations, and does not have a large systematic effect on the range of [O III] $\lambda 5007$ EWs.

The lower panel of Fig. 5 presents the dependence of the [O III] $\lambda 5007$ EW/CF on U , n_e and CF. The [O III] $\lambda 5007$ EW/CF represents the [O III] $\lambda 5007$ emissivity per unit solid angle of the NLR gas. This parameter ranges over a fac-

⁴ The apparently discrepant C IV $\lambda 1549$ NLR emission in type 2 and type 1 AGN is inconsistent with the inclination unification schemes for AGN, and this needs to be addressed in future studies.

tor of 5, which represents the amount of [O III] $\lambda 5007$ EW modulation by the combined effects of n_e and U . The NLR [O III] $\lambda 5007$ emissivity per unit solid angle is strongly correlated with U ($r_S = -0.800$, $Pr = 5.9 \times 10^{-10}$) and somewhat less strongly with n_e ($r_S = -0.708$, $Pr = 3.2 \times 10^{-7}$, again weakened by non detections). This emissivity is completely unrelated with CF ($r_S = -0.034$, $Pr = 0.83$). We finally note that n_e , U , and CF, are not significantly correlated with each other.

As expected (Section 4.1.3), essentially identical results were obtained with the modified soft SED. Somewhat stronger correlations were obtained in the two zone approximation. Specifically, the [O III] $\lambda 5007$ EW correlation with U rose to 0.454 and with CF_{out} to 0.778 (both parameters for the outer zone), while the correlations for the [O III] $\lambda 5007$ emissivity (Fig. 5, lower panel) remained essentially unchanged.

4.3 Relation with EV1 parameters

The [O III] $\lambda 5007$ line is one of the main components of the BG92 EV1 set of correlations. These correlations may be driven by some fundamental parameters, such as L/L_{Edd} (BG92). Below we briefly explore whether the NLR physical parameters n_e , U , and CF are correlated with some of the non-[O III] $\lambda 5007$ EV1 components (as listed in BG92).

The CF is significantly correlated with the absolute V band magnitude M_V ($r_S = 0.512$, $Pr = 7.6 \times 10^{-4}$), such that the CF decreases with increasing luminosity. This accounts for the tendency of the [O III] $\lambda 5007$ EW to decrease with increasing luminosity in the BG92 sample (note that Shemmer et al. 2004 do not find this effect in luminous high- z quasars). The only other parameter significantly correlated (i.e. $Pr < 10^{-2}$) with CF is the EW of the broad He II $\lambda 4686$ line ($r_S = 0.452$, $Pr = 3.4 \times 10^{-3}$). This correlation is not simple to interpret, and it may be induced by the strong inverse correlation of the broad He II $\lambda 4686$ EW with luminosity, and the above inverse correlation of luminosity and CF. Interestingly, there is no significant correlation of CF and L/L_{Edd} (taken from BL04; $r_S = -0.133$, $Pr = 0.41$). Such a relation was suggested by BG92 as the physical mechanism driving the set of EV1 correlations (see also Kraemer et al. 2004).

The n_e is significantly correlated with two surprising parameters, the soft X-ray slope ($r_S = -0.633$, $Pr = 1 \times 10^{-4}$), and the compact to total radio flux ratio from Kellermann et al. (1989) ($r_S = 0.560$, $Pr = 1.7 \times 10^{-4}$). A marginally significant correlation exists with the Fe II/H β flux ratio ($r_S = 0.415$, $Pr = 7.8 \times 10^{-3}$), which may point at a relation between the NLR density and the BLR metalicity.

The U is significantly correlated with the continuum luminosity at 3000 Å, and with the broad H β line FWHM, leading to a somewhat stronger, but hard to interpret correlation ($r_S = 0.552$, $Pr = 2.3 \times 10^{-4}$) with the estimated black hole mass (M_{BH} , see BL04). A stronger correlation exists with the Fe II/H β flux ratio ($r_S = -0.608$, $Pr = 3.1 \times 10^{-5}$). Again, this may point at a relation between the NLR ionization level and the BLR metalicity.

The two zone analysis yields similar correlations for CF_{out} with M_V ($r_S = 0.456$, $Pr = 3.1 \times 10^{-3}$), and with the broad He II $\lambda 4686$ EW ($r_S = 0.460$, $Pr = 2.8 \times 10^{-3}$). But, there are no significant correlations with CF_{in}. The cor-

relations for U_{out} are somewhat stronger than those for the single zone U (with M_{BH} , $r_S = 0.590$, $Pr = 6.1 \times 10^{-5}$; with Fe II/H β $r_S = 0.654$, $Pr = 4.8 \times 10^{-6}$).

4.4 The size of the NLR

The distance of the [O III] $\lambda 5007$ emitting region from the central ionizing continuum source, R_{NLR} , can be determined from the measured n_e and U for each object, and the estimated ionizing luminosity L_{ion} , as follows. By definition $U \equiv n_{\gamma}/n_e$, where the ionizing photon density is given by $n_{\gamma} = L_{\text{ion}}/4\pi R_{\text{NLR}}^2 c \langle h\nu \rangle$, where $\langle h\nu \rangle$ is the mean ionizing photon energy (3.03 Rydberg, for the CLOUDY MF ionizing continuum). These relations give $R_{\text{NLR}} = K L_{\text{ion}}^{1/2} (U n_e)^{-1/2}$, where $K \equiv (4\pi c \langle h\nu \rangle)^{-1/2}$.

Figure 6 presents the luminosity dependence of R_{NLR} for the single zone and for the two zone approximations. The correlation for the single zone is strong ($r_S = 0.836$, $Pr = 2 \times 10^{-11}$), with a best fit relation

$$R_{\text{NLR}} = 40 L_{44}^{0.45} \text{ pc},$$

where $L_{44} = \nu L_{\nu}(4861)/10^{44} \text{ erg s}^{-1}$. For the two zone approximation we get a somewhat weaker but still significant correlation of the size of the outer zone ($r_S = 0.648$, $Pr = 6 \times 10^{-6}$), with a best relation

$$R_{\text{NLR}}^{\text{out}} = 750 L_{44}^{0.34} \text{ pc}.$$

The assumption of fixed n_e and U values in the inner zone implies $R_{\text{NLR}}^{\text{in}} = L_{44}^{0.5} \text{ pc}$ by construction.

The single zone R_{NLR} versus L relation implies sizes which are much smaller than deduced through imaging of spatially extended [O III] $\lambda 5007$ emission in type 1 AGN with the *HST* (Bennert et al. 2002; Schmitt et al. 2003). For example, in four overlapping PG quasars (0026+129; 0053+251; 0953+414; 1307+085) Bennert et al. find $R_{\text{NLR}} = 2.2\text{--}5.9 \text{ kpc}$, while we get $R_{\text{NLR}} = 84\text{--}116 \text{ pc}$, i.e. about ~ 40 times smaller sizes. In the two zone approximation we get $R_{\text{NLR}}^{\text{out}} = 1.3\text{--}1.7 \text{ kpc}$, i.e. within a factor of 2-3 of the Bennert et al. values. However, the Bennert et al. *HST* images appear to be measuring the kpc-scale ‘extended NLR’ (ENLR, Unger et al. 1987), which according to the surface brightness values in Bennert et al. (Table 2 there), may include a significant component of unresolved [O III] $\lambda 5007$ emission. A more carefull analysis of these images is required to determine the fraction of unresolved [O III] $\lambda 5007$ emission, and the implied constraints on the [O III] $\lambda 5007$ radial emissivity distribution. Note also that the extrapolation of the Bennert et al. relation to higher L implies R_{NLR} values which are ruled out by ground based observations of high z quasars (Netzer et al. 2004), also pointing at a more compact R_{NLR} . Similarly, a compact NLR ($\lesssim 100 \text{ pc}$), consistent with our estimates, was deduced by Kraemer et al. (1998), based on detailed photoionization modeling of the narrow line emission in NGC 5548.

The slope of 0.45 for the single zone model implies that $U n_e$, i.e. n_{γ} is roughly constant. The scatter in the R_{NLR} versus L relation is only 0.2 (RMS in log R_{NLR}), which is significantly smaller than expected based on the measured range of values for U and for n_e ⁵. The small spread in the

⁵ Phenomenologically, this results from a weak anti-correlation

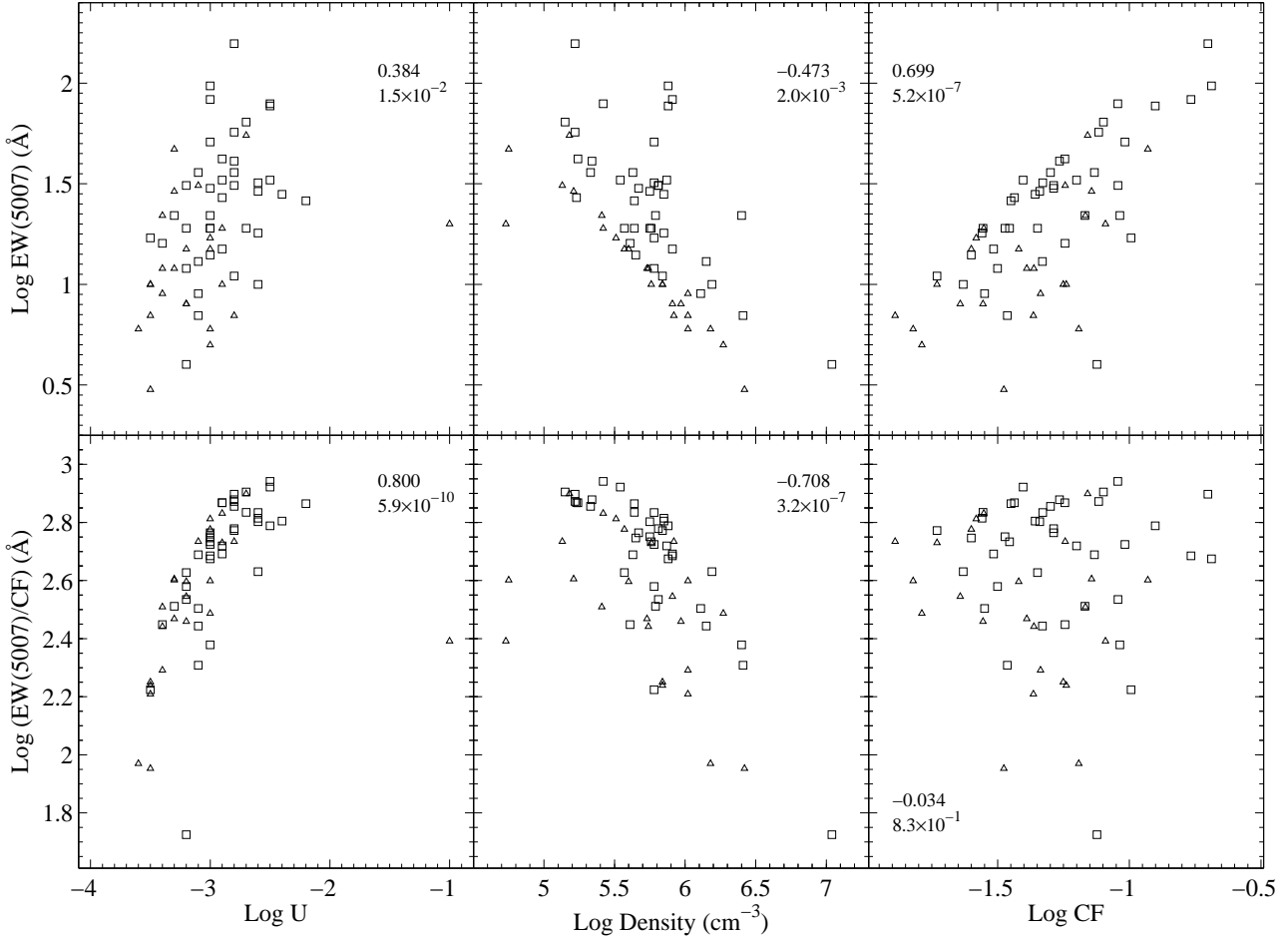


Figure 5. The dependence of [O III] $\lambda 5007$ EW (three upper panels) and [O III] $\lambda 5007$ /covering factor (three lower panels) on the ionization parameter, density and covering factor. The Spearman rank-order correlation coefficient (r_S) and the null probability (Pr) are indicated in each panel.

R_{NLR} versus L relation, and a slope close to 0.5, indicate a small spread of n_γ at the [O III] $\lambda 5007$ emitting region. It is not clear why such a small range in n_γ should be present⁶. The two zone model shows a somewhat larger scatter (0.3 RMS in $\log R_{\text{NLR}}^{\text{out}}$), and a flatter slope (0.34), which indicates a non-uniform n_γ .

The tight R_{NLR} versus L relation may be partly induced by the rejection of objects with non-detected [O III] $\lambda 4363$. In these objects, the arbitrary assumption that the true [O III] $\lambda 4363$ EW is 0.1 times the upper limit value leads to R_{NLR} values which are an order of magnitude larger than deduced for the rest of the objects. Thus, higher quality optical spectra, with complete detections of [O III] $\lambda 4363$, are required in order to measure more accurately the amount of scatter in the R_{NLR} versus L relation.

Figure 7 shows that there is also a significant inverse correlation between R_{NLR} and n_e ($r_S = -0.596$, $Pr = 4.9 \times 10^{-5}$). The slope of the relation is -0.56 . This relation is consistent with earlier findings of a negative radial

between U and n_e , which produces a smaller than expected dispersion in $U n_e$, compared to the dispersion in each parameter.

⁶ The small spread in the BLR n_γ can be understood in terms of the critical n_γ required for dust sublimation (e.g. LD).

density gradient in the NLR. In this case, inclusion of upper limits on [O III] $\lambda 4363$ as detections, at a tenth of their value, extends the correlation to large R_{NLR} and lower n_e , indicating that this correlation cannot be induced by ignoring the non detections.

Inspection of the correlations of R_{NLR} with the EV1 parameters yields that the broad H β FWHM is also correlated with R_{NLR} ($r_S = -0.494$, $Pr = 1.2 \times 10^{-3}$). This leads to a remarkably strong correlation of r_{NLR} with M_{BH} ($r_S = 0.744$, $Pr = 3.8 \times 10^{-8}$). This strong correlation stands in contrast with the lack of correlation of R_{NLR} with L/L_{Edd} ($r_S = -0.002$, $Pr = 0.99$). We note, however, that $R_{\text{NLR}}^{\text{out}}$ is not significantly correlated with M_{BH} ($r_S = 0.338$, $Pr = 3.3 \times 10^{-2}$). We do not have a simple plausible explanation for the strong R_{NLR} versus M_{BH} correlation. However, as mentioned above, one should note that this correlation is partly based on the R_{NLR} versus L relation, which needs to be verified with higher quality spectra allowing complete detections.

4.5 The CF of the NLR

Figure 8 presents a comparison of the single zone CF and the two zone CF_{in} and CF_{out}, for both the hard MF SED,

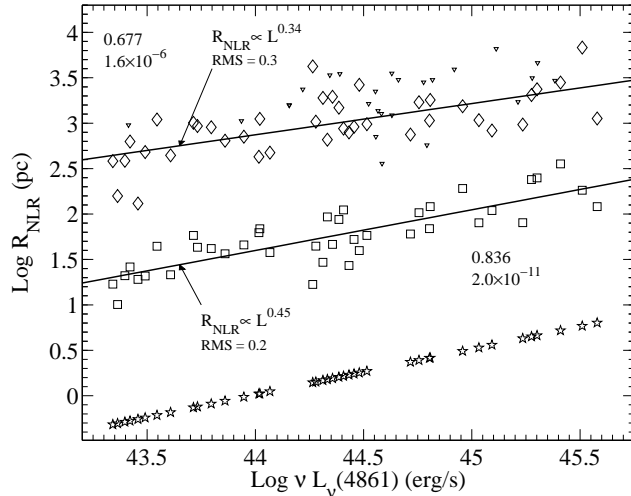


Figure 6. The luminosity dependence of R_{NLR} for the single-zone and two-zones models. Note the small scatter in the relation for the single-zone model (empty squares). A somewhat larger scatter is present for the outer zone in the two-zones model (detections-empty diamonds, triangles-upper limits). The radius of the inner region in the two-zones models (empty stars in the lower curve) follows an $L^{1/2}$ relation by construction. The upper curve indicates that most of the [O III] $\lambda 5007$ emission should be resolved with *HST* imaging.

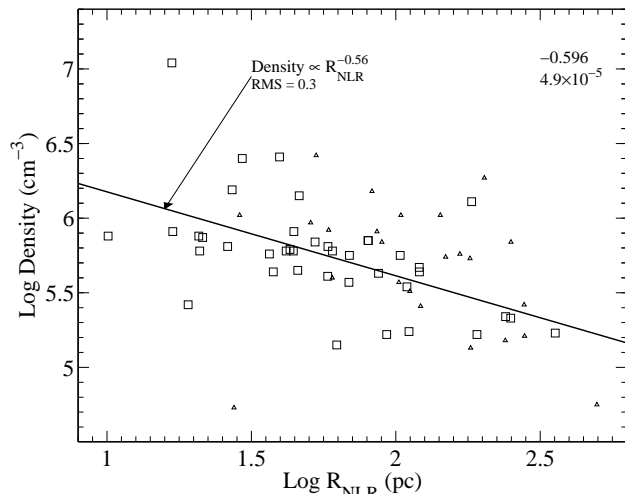


Figure 7. The radial gradient in NLR density. The objects with upper limits may have a larger R_{NLR} , and lower density, which would make this correlation stronger.

and for the softer -1.5 slope SED (Section 4.1.3). In the two zone model with the soft SED we require the inner zone to produce a similar [O III] $\lambda 4363$ /[O III] $\lambda 5007$ ratio as in the hard SED model, which lead to $\log U = -1.4$ for the inner zone (rather than $\log U = -1$ with the hard SED). As already noted above (Section 4.1.3), the softer SED implies CF values which are higher by 1.74 compared to the hard SED. A similar effect is seen in Fig. 8 for the two zone solution, where CF_{in} and CF_{out} in the soft SED solution are systematically higher than in the hard SED solution. For both SEDs CF and CF_{out} are rather well correlated, but CF_{in} can differ by a factor of 3-5 from CF. This is expected

since CF_{in} is largely set by [O III] $\lambda 4363$, while both CF and CF_{out} are largely set by [O III] $\lambda 5007$.

Independent constraints on the radial distribution of the covering factor of dusty gas in the NLR can be obtained from models for the IR SED of AGN. In the two zone model, the inner zone is within a factor of few of the dust sublimation radius (e.g. Fig. 8 in LD), and the associated dust radiation should thus peak at $\sim 3-5 \mu\text{m}$, while the outer zone is at a ~ 750 larger radius, and should thus peak at $\sim 50-100 \mu\text{m}$. The ratio $\text{CF}_{\text{out}}/\text{CF}_{\text{in}}$ should then determine the shape of the far to near IR SED. Interestingly, Fig. 8 indicates that this ratio is systematically different for the soft and the hard SEDs, which suggests one may be able to obtain constraints on the ionizing SED based on the observed NLR emission and IR SED. The two zone model presented here is obviously highly simplified, and a more realistic model should invoke a continuous radial distribution of dusty gas.

As discussed earlier, the large fraction of bolometric luminosity emitted in the IR ($\sim 0.3-0.5$ in typical AGN), requires a correspondingly large CF of dusty gas (e.g. Sanders 1989). Earlier studies noted that the CF deduced based on the EW of NLR non-resonant recombination lines is only a few percent, and concluded that there must exist an additional NLR component with a large CF and $U \gg 10^{-2}$ (Voit 1992; LD, Netzer & Laor 1993). Our single zone model yields $\log \text{CF} \sim -1 \pm 0.5$ (for the soft SED), which is still too low. A somewhat larger total CF is obtained with the two zone model, mainly due to our assumption of $\log U = -1$ in the inner zone. As briefly mentioned in Section 2, some of our solutions with $\log U < -2.2$ will be degenerate with models with $\log U > -1$ (Fig. 3). Such high U models will require a higher CF, which may be in better agreement with the IR constraints on the CF. However, the best test for such high U models is through the various expected high ionization lines (originating in the surface layer where dust absorption is negligible).

Finally, we note that the [O III] $\lambda 5007$ line is one of the main NLR coolants over a rather wide range of n_e and U (e.g. Ferguson et al. 1997), and thus should be a good tracer for most of the NLR gas. The [O III] $\lambda 5007$ line becomes a negligible coolant at $\log U < -3.5$ (e.g. Fig. 3), once most O is in O I and O II forms. However, a large covering factor of low U NLR gas without [O III] $\lambda 5007$ emission can be ruled out in most objects based on the following argument. Such a low U component would account for a significant fraction of the H β line EW, and thus the inferred [O III] $\lambda 5007$ /H β ratio in the [O III] $\lambda 5007$ emitting region will be significantly larger than the observed ratio. The commonly observed ratio of [O III] $\lambda 5007$ /H $\beta \sim 10$ is already quite close to the maximum possible value in photoionization models (e.g. Fig. 2, upper panel), and it does not allow more than $\sim 1/2$, of the H β line to originate in non [O III] $\lambda 5007$ emitting gas.

5 CONCLUSIONS

We use the [O III] $\lambda 5007$ line profile to measure the EW of the [O III] $\lambda 4363$ and H β emission lines in the BG92 sample of bright $z < 0.5$ AGN. All three lines are detected in 40 out of the 78 sample objects where optical spectra are available. The EW of the three lines are used, together with photoion-

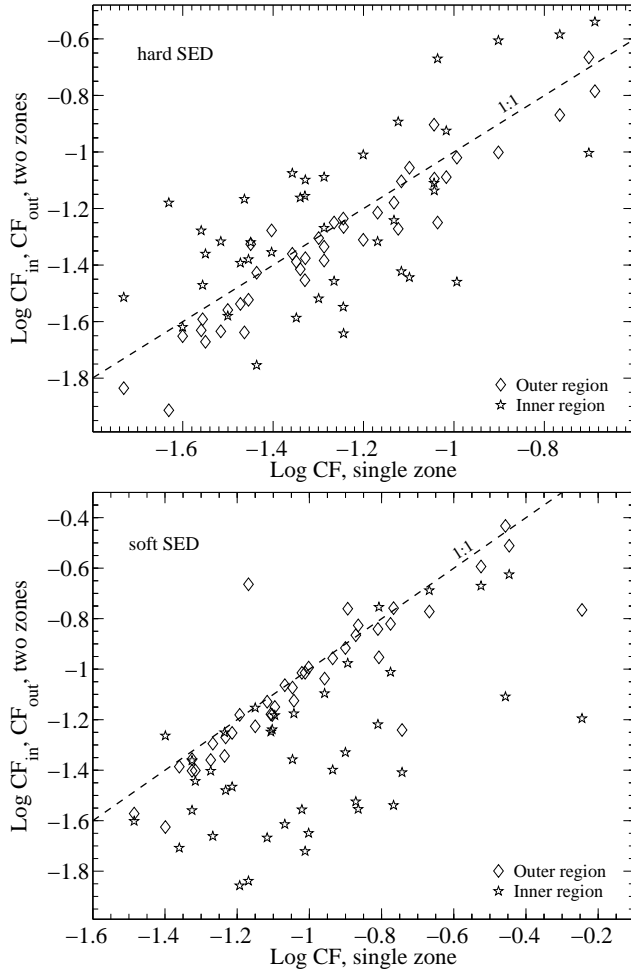


Figure 8. The covering factor of the outer (empty diamond) and inner (empty star) regions in the two-zones model versus the covering factor of the single-zone model. Upper panel, the relation for the assumed hard ionizing MF SED. Lower panel, the relation for the soft ionizing SED. A 1:1 relation is denoted by the dashed line in both panels. Note that that the ratio CF_{in}/CF_{in} in a given object, which sets the observed IR SED, is a function of the ionizing SED.

ionization models, to infer n_e , U , and CF of the [O III] $\lambda 5007$ emitting gas in the NLR. We find the main following results:

1. The inferred n_e and U in the single zone approximation show a relatively small range ($n_e \sim 10^5 - 10^{6.5} \text{ cm}^{-3}$, $U \sim 10^{-2.5} - 10^{-3.5}$), which corresponds to the range where the [O III] $\lambda 5007$ emissivity is maximized.

2. The strength of the [O III] $\lambda 5007$ line is mostly modulated by the range of CF of the photoionized gas. The range of [O III] $\lambda 5007$ emissivity per unit solid angle, set by n_e , and U , accounts for about half the range produced by the CF. Similar results are obtained for soft and hard ionizing SEDs, and for an extreme two zone approximation for the NLR.

3. The NLR CF is inversely correlated with luminosity, consistent with some earlier suggestions, but it is not correlated with L/L_{Edd} , unlike earlier suggestions.

4. We find a rather tight radius luminosity relation, $R_{\text{NLR}} = 40L_{44}^{0.45} \text{ pc}$, in the single zone approximation. We also find an unexpected strong correlation of R_{NLR}

and M_{BH} . However, both relations may be induced by our [O III] $\lambda 4363$ detection limits.

5. The observed line ratios can also be fit with a two zone model, where most of [O III] $\lambda 5007$ originates in an $n_e = 10^3 \text{ cm}^{-3}$ component at $R_{\text{NLR}}^{\text{out}} = 750L_{44}^{0.34} \text{ pc}$, and most of [O III] $\lambda 4363$ in an $n_e = 10^7 \text{ cm}^{-3}$ component at $R_{\text{NLR}}^{\text{in}} = L_{44}^{0.5} \text{ pc}$. Significant constraints on the spatial distribution of the [O III] $\lambda 5007$ emission can be obtained through *HST* imaging of luminous type 1 AGN, which should be able to resolve most of the [O III] $\lambda 5007$ emission if it occurs in $n_e \sim 10^3 \text{ cm}^{-3}$ gas.

Significantly higher quality optical spectroscopy of AGN, allowing complete detections of the [O III] $\lambda 4363$ line, is required to establish the strength of the R_{NLR} correlations with L and M_{BH} .

Independent constraints on the radial distribution of the NLR gas covering factor can be deduced from the IR SED. These constraints, together with measurements of lower and higher ionization narrow lines, and more realistic photoionization models involving a radial distribution of dusty gas (e.g. Ferguson et al. 1997), can provide a better understanding of the origin of the observed extreme range in narrow line strengths in AGN.

ACKNOWLEDGMENTS

We thank H. Netzer for the many helpful comments. We also thank T. Boroson for providing the optical spectra and accurate redshifts for all objects, Z. Shang for providing optical spectra, M.-P. Véron-Cetty for providing the I Zw 1 spectra, and G. Ferland for making the photoionization code CLOUDY publicly available. This research was supported by THE ISRAEL SCIENCE FOUNDATION (grant #1030/04), and by a grant from the Norman and Helen Asher Space Research Institute.

REFERENCES

- Baskin A., Laor A., 2004, MNRAS, in press (BL04)
- Bennert, N., Falcke, H., Schulz, H., Wilson, A. S., & Wills, B. J. 2002, ApJ, 574, L105
- Binette, L., Wilson, A. S., & Storchi-Bergmann, T. 1996, A&A, 312, 365
- Boroson A. T., Green R. F., 1992, ApJS, 80, 109 (BG92)
- Dopita, M. A., Groves, B. A., Sutherland, R. S., Binette, L., & Cecil, G. 2002, ApJ, 572, 753
- Ferguson, J. W., Korista, K. T., Baldwin, J. A., & Ferland, G. J. 1997, ApJ, 487, 122
- Ferland, G. J., Korista, K. T., Verner, D. A., Ferguson, J. W., Kingdon, J. B., & Verner, E. M. 1998, PASP, 110, 761
- Ferland, G. J. & Osterbrock, D. E. 1986, ApJ, 300, 658
- Groves, B. A., Dopita, M. A., & Sutherland, R. S. 2004a, ApJS, 153, 9
- Groves, B. A., Dopita, M. A., & Sutherland, R. S. 2004b, ApJS, 153, 75
- Heckman, T. M., Miley, G. K., van Breugel, W. J. M., & Butcher, H. R. 1981, ApJ, 247, 403
- Kellermann, K. I., Sramek, R., Schmidt, M., Shaffer, D. B., & Green, R. 1989, AJ, 98, 1195

Kraemer, S. B., Crenshaw, D. M., Filippenko, A. V., & Peterson, B. M. 1998, ApJ, 499, 719

Kraemer, S. B., George, I. M., Crenshaw, D. M., & Gabel, J. R. 2004, ApJ, 607, 794

Laor A., Draine B. T., 1993, ApJ, 402, 441(LD)

Laor, A., Fiore, F., Elvis, M., Wilkes, B. J., & McDowell, J. C. 1997, ApJ, 477, 93

Mathews, W. G. & Ferland, G. J. 1987, ApJ, 323, 456 (MF)

Moore C. E., 1993, Tables of Spectra of Hydrogen, Carbon, Nitrogen, and Oxygen Atoms and Ions. CRC Press, Boca Raton, Florida

Nagao, T., Murayama, T., & Taniguchi, Y. 2001, ApJ, 549, 155

Netzer, H. & Laor, A. 1993, ApJ, 404, L51

Netzer, H., Shemmer, O., Maiolino, R., Oliva, E., Croom, S., Corbett, E., & di Fabrizio, L. 2004, ApJ, 614, 558

Neugebauer G., Green R. F., Matthews K., Schmidt M., Soifer B. T., Bennett J., 1987, ApJS, 63, 615

Osterbrock, D. E. 1989, Astrophysics of gaseous nebulae and active galactic nuclei, Publisher: University Science Books, Mill Valley, CA.

Peterson, B. M. 1997, An introduction to active galactic nuclei, Publisher: Cambridge, New York Cambridge University Press, 1997

Pradhan A. K., Peng J., 1995, in Space Telescope Science Institute Symposium Series No. 8, ed., Williams R.E., Livio M., Cambridge Univ. Press

Sanders, D. B., Phinney, E. S., Neugebauer, G., Soifer, B. T., & Matthews, K. 1989, ApJ, 347, 29

Schlegel D. J., Finkbeiner D. P., Davis M., 1998, ApJ, 500, 525

Schmidt M., Green R. F., 1983, ApJ, 269, 352

Schmitt, H. R., Donley, J. L., Antonucci, R. R. J., Hutchings, J. B., Kinney, A. L., & Pringle, J. E. 2003, ApJ, 597, 768

Scott, J. E., Kriss, G. A., Brotherton, M., Green, R. F., Hutchings, J., Shull, J. M., & Zheng, W. 2004, ApJ, 615, 135

Seaton M. J., 1979, MNRAS, 187, 73P

Shang Z., Wills B. J., Robinson E. L., Wills D., Laor A., Xie B., Yuan J., 2003, ApJ, 586, 52

Shemmer, O., Netzer, H., Maiolino, R., Oliva, E., Croom, S., Corbett, E., & di Fabrizio, L. 2004, ApJ, 614, 547

Unger, S. W., Pedlar, A., Axon, D. J., Whittle, M., Meurs, E. J. A., & Ward, M. J. 1987, MNRAS, 228, 671

Vanden Berk, D. E., et al. 2001, AJ, 122, 549

Véron-Cetty, M.-P., Joly, M., Véron, P. 2004, A&A, 417, 515

Voit, G. M. 1992, ApJ, 399, 495

Wills, B. J., Netzer, H., Brotherton, M. S., Han, M., Wills, D., Baldwin, J. A., Ferland, G. J., & Browne, I. W. A. 1993, ApJ, 410, 534

Zheng, W., Kriss, G. A., Telfer, R. C., Grimes, J. P., & Davidsen, A. F. 1997, ApJ, 475, 469